RMetS

Royal Meteorological Society

Wind waves climatology of the Southeast Pacific Ocean

Catalina Aguirre,[a,c]* José A. Rutllant[b,d] and Mark Falvey[b]

[a] *School of Ocean Engineering, Faculty of Engineering, Universidad de Valparaíso, Valparaíso, Chile*
[b] *Department of Geophysics, Faculty of Physical and Mathematical Sciences, Universidad de Chile, Santiago, Chile*
[c] *Center for Climate and Resilience Research, Universidad de Chile, Santiago, Chile*
[d] *Center for Advanced Studies in Arid Zones, La Serena, Chile*

ABSTRACT: The climatology of wind waves over the Southeast Pacific is analysed using a 32-year hindcast from the WaveWatch III model, complemented by satellite-derived significant wave height (SWH) and buoy measurements for validation. Using partitioned spectral data, a regional climatology of wind sea and swell parameters was constructed. In general, the simulated SWH shows a good agreement with satellite and *in situ* SWH measurements, although the model appears to have a spatially uniform bias of approximately 0.3 m. The spatial pattern of SWH is clearly influenced by the meridional variation of mean surface wind speed, where the stronger winds over the Southern Ocean play a significant role generating higher waves at higher latitudes. Nevertheless, regional features are observed in the annual variability of SWH, which are associated with the existence of atmospheric coastal low-level jets off the coast of Peru and central Chile. In particular, the seasonal variation of these synoptic scale jets shows a direct relationship with the annual variability of SWH and with the probability of occurrence of wind sea conditions. Off the coast of Peru at approximately 15°S the coastal low-level jet is strongest during austral winter, increasing the wind sea SWH. In contrast, off central Chile, there is an important increase of wind sea SWH during summer. The seasonal variation of the wind sea component leads to a contrasting seasonal variation of the total SWH at these locations: off Peru the coastal jet amplifies the annual variability of SWH, while off Central Chile the annual variability of SWH is suppressed by the presence of the coastal jet. Although the general conclusions of this research are considered to be robust, we discuss the limitations of the spectral partitioning method used to distinguish wind sea and swell-sea states.

KEY WORDS   wave climatology; swell; wind sea; atmospheric low-level coastal jets; Southeast Pacific

Received 6 June 2016; Revised 10 March 2017; Accepted 12 March 2017

1. Introduction

Wind waves contain more than half of the energy of all ocean surface waves, more even than tsunamis or tides, due to their ubiquitous presence over the oceans. Wind waves (hereafter waves) play a major role in many processes at the air–sea interface (Donelan *et al.*, 1997; Fan *et al.*, 2009; Cavaleri *et al.*, 2012) and in the coastal environment (Komar, 1997). Thus, their climatological behaviour is of interest to both the scientific and coastal engineering communities. Since the first global maps of satellite-based wave height measurements were presented by Chelton *et al.* (1981), several global-scale wave climatologies have been constructed using remotely sensed (Young, 1999) or visual observations (Gulev *et al.*, 2003). For example, satellite altimetry data have been used to determine the global distribution of significant wave height (SWH) and to estimate long-term wave height trends and extremes (Izaguirre *et al.*, 2011; Young *et al.*, 2011).

The use of numerical wave simulations forced by global wind data from atmospheric reanalysis (hindcasts) has become a popular method to assess global wave climate

(Sterl *et al.*, 1998; Cox and Swail, 2001; Sterl and Caires, 2005). In recent years, several updated wave climatologies have been published based on newly available wind reanalysis (Chawla *et al.*, 2013; Rascle and Ardhuin, 2013; Durrant *et al.*, 2013). Fan *et al.* (2012) have presented a fully coupled global wave simulation using a coupled atmosphere-wave model. Furthermore, numerical wave models have been used to examine possible changes in the global wave climate under global warming scenarios (Semedo *et al.*, 2013, Hemer *et al.*, 2013a, Fan *et al.*, 2013).

There are also many examples of observational and modelling studies that have been performed to describe wave climate at regional scales. Most of these have examined coastal regions in the Northern Hemisphere (Allan and Komar, 2000; Woolf *et al.*, 2002; Dodet *et al.*, 2010; Reistad *et al.*, 2011). Apart from the hemispheric study of Hemer *et al.* (2010) who described the interannual wave variability, very few studies have assessed regional wave climate in the Southern Hemisphere, where past work has mostly focused on the coasts of Australia and New Zealand (Laing, 2000; Gorman *et al.*, 2003; Bosserelle *et al.*, 2011). To our knowledge, the Southeast Pacific coast still lacks a high-resolution hindcast and a detailed description of its wave climatology. Since buoy wave measurements are particularly scarce along the coast of South

---

* Correspondence to: C. Aguirre, Department of Ocean Engineering, Valparaiso University, Avenida Brasil 1786, Valparaiso, Chile. E-mail: catalina.aguirre@uv.cl

America, a model hindcast forced with wind information derived from atmospheric reanalysis seems an attractive way to generate a wave climatology in this region, providing far better spatial and temporal coverage than can be achieved using observational data alone. BAIRD & Associates Coastal Engineering Ltd. have performed a 12-year hindcast (1985–2005) for the entire Pacific Ocean forced by National Center for Environmental Prediction (NCEP) reanalysis winds at 2° spatial resolution corrected with QuikSCAT winds (www.olasdelpacifico.com). Nevertheless, these data are not in the public domain, being only available to other engineering entities. Other efforts in the region have been mostly related with prospection of wave energy. For instance, Mediavilla and Sepuvelda (2016) estimated wave energy resources for the near-shore area of central Chile (~33°S) during the period 2009–2010 using a very high spatial resolution.

The Southeast Pacific coast is particularly interesting due to its large latitudinal range that extends from the tropics to the southernmost tip of South America in the Southern Ocean where the global maximum SWH is observed (Young, 1999). The South American west coast exhibits distinct near-surface wind climates depending on latitude. While south of 40°S the coast is year-round exposed to the westerly wind belt and associated synoptic scale disturbances, to the north the prevailing winds are mostly driven by the subtropical Southeast Pacific Anticyclone (SPA). Off the coast of Peru (~15°S), along-shore winds are equatorward year-round with maximum speeds in austral winter (Dewitte *et al.*, 2011). Off the coast of northern Chile (~18°–28°S) equatorward winds are weaker and exhibit little synoptic and seasonal variability (Pizarro *et al.*, 1994). Along the coast of central Chile (~28°–40°S) coastal winds exhibit a marked seasonal and synoptic scale modulation with mean southerly along-shore winds alternating from moderate in winter to strong during spring and summer, following the seasonal latitudinal migration of the SPA (Rahn and Garreaud, 2013). The synoptic variability during spring and summer is mainly due to an alternation between southerly coastal atmospheric low-level jet events (Garreaud and Munoz, 2005) and periods of weak southerlies or even northerly flow in connection with the passage of coastal lows (Garreaud *et al.*, 2002). This seasonal and synoptic-scale variability in surface winds have shown to significantly impact the surface ocean circulation and sea surface temperature (Renault *et al.*, 2009, 2012, Aguirre *et al.*, 2012, 2014). Therefore, it is also expected that these regional near-surface wind patterns along the west coast of South America will have an impact on the wave climate.

Although SWH is the most commonly used parameter to describe waves, it is not able to distinguish between different sea states. The co-existence of swells (waves forced remotely) and wind sea (waves forced by local wind) could lead to the same SWH. Thus, the separate analysis of wind sea and swell contributions to SWH provides a better understanding of the factors that determine the variability of the wave field. For this reason, many studies have focused on the wind sea and swell separately. Using visual data from the Voluntary Observing Ship

programme, large-scale climatologies of swell and wind sea parameters have been constructed (Gulev *et al.*, 2003). Semedo *et al.* (2011) used a 45-year hindcast to assess the global wind sea and swell climatology, and noted the impact of locally enhanced winds at the coasts where atmospheric low-level jets are present. Furthermore, global projections of wind sea and swell under climate change scenarios have been assessed by Fan *et al.* (2014).

In this article, we use a 32-year high-resolution hindcast to examine the wave climatology of the Southeast Pacific and determine the impact of the regional atmospheric circulation features on the wave parameters and the sea state. The specific study area may be defined as the region approximately 1000 km from the Southeast Pacific coast between the latitudes of 5°S (northern border of Peru) and 56°S (Cape Horn). For validation purposes, we consider satellite-derived SWH data and available *in situ* observations. The article is organized as follows: in Section 2 we describe the model configuration, satellite data and *in situ* observations. A validation of the model is presented in Section 3. In Section 4, we present the climatology constructed for the Southeast Pacific. A discussion of some aspects of the results is included in Section 5 along with concluding remarks.

2. Model and observations

2.1. Model configuration

The model used in this study is the Wavewatch III version 3.14 (Tolman, 2009), which is a third generation spectral wind wave model developed by the NCEP. This model supports the use of two-way nested grids and as such is a good choice for regional studies where high-resolution results over limited areas are desirable (Tolman, 2008).

We carried out a simulation for the Pacific Ocean basin, from 116°E to 64°W in longitude and from 66°N to 80°S in latitude, with a spatial resolution of 0.5°. This parent grid contained an embedded higher resolution grid (0.16°) for the Southeast Pacific, from 85° to 65°W in longitude and from 0° to 59°S in latitude (Figure 1(a)). While it is possible that some source regions of remotely generated swells are outside of the parent domain, such as the Indian and South Atlantic Ocean, we believe that these swells do not have a significant impact on the climatology of the Southeast Pacific. For example, Alves (2006) shows that extratropical areas of the Indian Ocean do spread wave energy throughout the Pacific Ocean, but with a very low persistence in the Southeast Pacific. Extratropical areas of the South Atlantic Ocean are also able to generate robust swell systems that propagate westward against the dominant storm tracks. However, this could affect only the very southern limit of our domain and unlikely to have a significant impact over most of the Southeast Pacific.

To generate both grids we used the automated grid generation tools for Wavewatch III (Chawla and Tolman, 2007) that uses bathymetry from the General Bathymetric Chart of the Oceans (GEBCO) with a one arc-minute grid interval. The shoreline data used was the Global
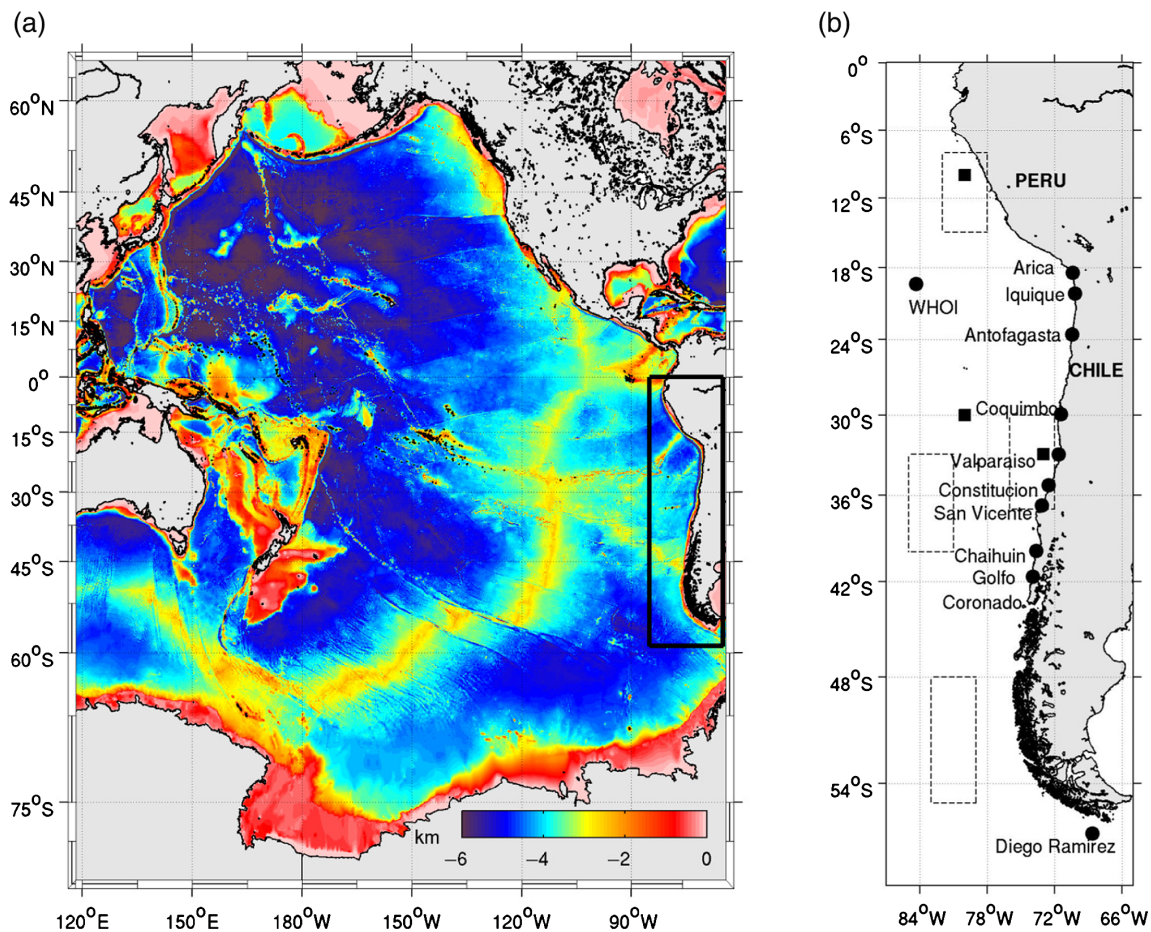
Figure 1. (a) Pacific Ocean (outer domain) with GEBCO bathymetry used in the WW3 simulation and (b) inner domain for the Southeast Pacific. Buoy measurement locations are denoted by dots (●) and locations with spectral data are denoted by squares (■). In addition, regions off Peru, near-shore central Chile, offshore central Chile and off Patagonia are demarked by dashed rectangles (▬ ▬). [Colour figure can be viewed at wileyonlinelibrary.com].

Self-Consistent Hierarchical High-Resolution Shoreline (GSHHS) with resolutions of 5 km for the outer grid and 1 km for the inner grid. To force the model, we used sea ice and wind fields 10 m above the sea surface with a temporal resolution of 6 h and a spatial resolution of 0.313° from the Climate Forecast System Reanalysis (CFSR, Saha *et al.*, 2010). This data set is generated from a coupled atmosphere, ocean circulation, land surface and sea ice model. One of the major advantages of using this data set is its relatively high spatial resolution, allowing for a more detailed representation of the near-surface coastal wind features off western South America (Rahn and Garreaud, 2013). In addition, CFSR data have been applied successfully in recent wave hindcast described by Chawla *et al.* (2013). To test if CFSR data (0.3° spatial resolution) adequately capture the coastal jets, we compared these data with a regional atmospheric simulation of 6 km spatial resolution off central Chile using the Weather Research and Forecasting model (Skamarock *et al.*, 2008). Results showed that in spite of their lower spatial resolution, the low-level coastal jet is well represented in CFSR data. Thus, the use of the output of a high-resolution atmospheric model to drive the ocean regional domain would not modify the results significantly.

The model spectral domain was discretized into 29 frequencies from 0.035 to 0.505 Hz with an increment factor of 1.1, and 24 regularly spaced directions (15° intervals). Parametrizations used include the following: (1) the Tolman–Chalikov source term package with stability correction (Tolman and Chalikov, 1996), (2) the discrete interaction approximation to simulate nonlinear wave–wave interactions (Hasselmann *et al.*, 1985), (3) dissipation due to bottom friction using the JON-SWAP formulation (Hasselmann *et al.*, 1973) and (4) the depth-induced wave breaking using the Battjes and Janssen formulation, with a Miche-style shallow water limiter for maximum energy (Battjes and Janssen, 1978).

Using this configuration a 32-year hindcast was carried out for the period between 1979 and 2010. Gridded SWH, mean wave period (MWP) and mean wave direction (MWD) were saved at hourly intervals, while spectral data along the coast were saved every 6 h. The wave partitioning allows the identification of swells and wind sea from directional wave spectra, dividing it into subsets and calculating statistics for each subset. Here, the wave spectral partitioning method of Hanson and Phillips (2001), which is adapted from the approach of the Hasselmann *et al.* (1994), was used. The detailed implementation of

this partitioning method in WaveWatch III is described in Tracy *et al.* (2007). First, the method isolates energy peaks in the spectral data, and then uses a wave age criterion to identify wind seas, such that sea peaks lie within the parabolic boundaries defined by

$$f_p \geq \frac{g}{2\pi} \left[C_{mult} U_{10} \cos \delta \right]^{-1} \quad -\frac{\pi}{2} \leq \delta \leq \frac{\pi}{2}$$

where, f_p is the peak frequency of the wind sea in deep water, g is acceleration of gravity, C_{mult} is a wave age factor, U_{10} is the 10 m wind speed, and δ is the angle between the wind and wind sea. This relationship defines a parabolic region over the spectral matrix and any peak that falls within this region is considered to be forced by the wind and defined as 'wind sea'. Peaks that fall outside this region are considered to be 'swell'. Here, K is set to 1.7 following Tracy *et al.* (2007) to allow for nonlinear interactions that shift the boundary to lower frequencies. Statistics of wind sea and primary swell were saved each 3 h.

2.2. Satellite observations and data processing

Altimeter derived SWH data were obtained from the Radar Altimeter Database System (RADS) of the Delft University of Technology (Scharroo *et al.*, 2013). Here, we used data from the Ku-band altimeters ERS-1, ERS-2, TOPEX, JASON, ENVISAT and GFO. We follow the methodology of Woolf *et al.* (2002) and Hemer *et al.* (2010) to generate a $2° \times 2°$ regular latitude-longitude mesh with monthly temporal resolution from 1993 to 2015.

The RADS environment provides quality flags for all measurements. To construct our regular grid, all flagged data were discarded. In addition, data out of the $0 - 20$ dB range in the radar backscatter or with a wave height standard deviation higher than 0.1 m range were also rejected, as high values indicating returns may be contaminated by rain (Hemer *et al.*, 2010). Since reliable satellite-derived wave height data requires calibration using *in situ* measurements (Woolf *et al.*, 2002), we have used the calibration proposed by Challenor and Cotton (2002) for ERS-1, ERS-2 and TOPEX altimeters, and the calibration proposed by Queffeulou (2004) for JASON, GFO and ENVISAT altimeters. A summary of the wave height calibration equations can be found in Table 1. Occasional gaps in the maps of SWH occur for a few grid points due to the sparse sampling by the altimeter. These gaps are filled using linear interpolation and finally the data is smoothed using a 5×5 cell Gaussian digital filter.

In addition, we construct a climatology using 7 years of SWH derived from altimetry from 2009 to 2015. Daily maps in a Mercator grid of $1°$ spatial resolution are distributed by AVISO (archiving, validation and interpretation of satellite oceanographic data).

2.3. In situ observations

Ten coastal-buoy records are available from Servicio Hidrográfico y Oceanográfico de la Armada de Chile (SHOA, Figure 1(b)). Although their low spatial and temporal coverage prevent these records from being useful for

the direct assessment of wave climate, they do represent a valuable source of information in order to validate the model simulation. Time series for each buoy have a temporal resolution of 3 h. However, measurements were not simultaneous, as listed in Table 2. In addition, hourly data available online from one offshore buoy operated by the Woods Hole Oceanographic Institution (WHOI: station 32012) were used (Figure 1(b)). These data were obtained from http://www.ndbc.noaa.gov/.

2.4. Spectral data

Additional spectral data were obtained from a wave hindcast between 1979 and 2010 using the model WaveWatch III forced with CFSR hourly winds and sea ice, performed by the Collaboration for Australian Weather and Climate Research (CAWCR, Durrant *et al.*, 2013). The complete data set contains spectral wave outputs at 3683 points of which we have used only one off Peru ($10°S - 80°W$) and another offshore central Chile ($30°S - 80°W$). In addition, spectral data close to the coast at Valparaíso ($\sim 33°S$) are obtained by our simulation (Figure 1(b)). We expect consistency between the CAWCR and our data sets, since they are simulated using the same model, forced with the same wind and sea ice reanalysis and with similar parametrizations, except that the CAWCR simulation uses the source terms parameterizations ST4 of Ardhuin *et al.* (2010).

3. Validation

In this section, we evaluate the quality of the simulated SWH using the satellite altimeter and *in situ* measurements described previously in Sections 2.2 and 2.3.

3.1. Comparison of the simulated SWH against altimeter data

Figure 2 presents maps of the mean SWH (1992–2010), along with the bias, scatter index (SI) and temporal correlation (R) derived from the comparison between the simulated and altimeter SWH data. To construct these maps, the model data were monthly averaged and interpolated on to a $2° \times 2°$ grid to match the spatial and temporal scale of the altimeter data.

The spatial patterns of the simulated and satellite-derived mean SWH are in close agreement (Figures 2(a) and (b)). However, the bias map (Figure 2(c)) shows that the model mean SWH is generally higher than the satellite-derived mean SWH, with a spatially uniform bias between 0.2 and 0.3 m over the whole domain. This appears to be consistent with the results of other authors. For example, in a global simulation performed by Cox and Swail (2001) the strongest bias was found in the Southeast Pacific with values between 0.25 and 0.5 m. More recently, Fan *et al.* (2012) found a bias of 0.27 m in the Southeast Pacific using a coupled atmosphere-wave model. This bias pattern is most likely caused by inadequate swell dissipation formulation in ST2 parametrization, which scales with friction velocity and thus vanishes when the

Table 1. Altimeter data and wave height calibration.

Altimeter	Calibration	Dates	Reference
ERS-1	$H = 1.109 H_{ERS-1} + 0.334$	August 1991–June 1996	Challenor and Cotton (2002)
ERS-2	$H = 1.061 H_{ERS-2} + 0.035$	June 1995–June 2003	Challenor and Cotton (2002)
TOPEX	$H = 1.052 H_{TOPEX} - 0.094 \ (-0.0004D)^*$	October 1992–September 2005	Challenor and Cotton (2002)
JASON	$H = 1.059 H_{JASON} - 0.057$	January 2002–June 2013	Queffeulou (2004)
GFO	$H = 1.0625 H_{GFO} + 0.075$	January 2000–July 2008	Queffeulou (2004)
ENVISAT	$H = 1.0526 H_{ENVISAT} - 0.199$	June 2002–July 2011	Queffeulou (2004)

*In the calibration of TOPEX, D is the number of days since 26 September 1996. It is zero prior to 26 September 1996 and after to 31 August 2002.

Table 2. Buoy data used to validate the model in the Southeast Pacific region.

Site name	Latitude (°S)	Longitude (°W)	Start time	End time
32012 (WHOI)	19°22.6′	84°22.2′	29 October 2007	21 July 2010
Arica	18°27.3′	70°22.8′	07 July 1988	06 July 1989
Iquique	20°10.9′	70°10.3′	05 June 1986	12 July 1987
Antofagasta	23°35.6′	70°25.6′	15 October 1990	05 December 1991
Coquimbo	29°55.7′	71°22.6′	17 August 1989	10 October 1990
Valparaíso	32°59.7′	71°49.5′	01 January 2010	10 October 2010
Constitución	35°17.0′	72°31.5′	18 February 1984	22 February 1985
San Vicente	36°43.9′	73°9.2′	29 November 1985	05 February 1986
Chaihuin	39°55.1′	73°38.2′	18 April 1985	28 June 1985
Golfo Coronado	41°40.0′	73°56.52′	13 May 1986	11 July 1987
Diego Ramírez	56°32.5′	68°38.0′	31 May 1981	10 January 1984

wind ceases. This seems to be unrealistic and a new set of parameterizations for the dissipation source terms of the wave energy balance equation have been proposed and implemented in the latest versions of Wavewatch III (Ardhuin *et al.*, 2010; Babanin, 2011), suppressing the SWH overestimation. Nevertheless, comparison of SWH variability using different source term parametrizations show similar results in centred root-mean-square (RMS) error and correlation values (Stopa *et al.*, 2016). Thus, we expect that the bias found in our simulated SWH does not change the overall conclusions of this research.

The SI is calculated by dividing the RMS error by the mean of the simulated SWH at each grid point and multiplying it by 100. It represents the RMS error as a percentage of its mean value. In general, the SI map shows RMS errors smaller than 10% south of approximately 27°S, while errors close to 15% are observed in the northernmost part of the study domain. The linear correlation coefficient (R) map shows values typically above 0.9, except in the coastal region, particularly off the coast of central Chile, where the correlation drops to about 0.8 (Figure 2(e)).

3.2. Comparison of the model against buoy data

To assess the performance of the model on shorter time scales, the *in situ* data were compared with the model results interpolated to the buoy locations. In general, raw data were used and only small-time gaps were linearly interpolated. Table 3 shows summary statistics [bias, the SI, the linear correlation coefficient R, the linear regression slope (m) and the *y*-axis intercept (b)] that describe model performance for the simulated SWH and MWP, defined as

the second moment wave period (Tm02),

$$Tm02 = \sqrt{\frac{\iint E(f,\theta)\,df d\theta}{\iint f^2 E(f,\theta)\,df d\theta}}$$

In addition, Figure 3 shows scatter plots for selected buoys (Valparaiso and WHOI), where measurements are more recent, and a time series of the MWD at the Valparaíso station, the only directional buoy available.

In general, the model shows better performance for the SWH than for the MWP. The SWH exhibits correlation coefficients in the range 0.77–0.85 (except in San Vicente), while the MWP shows correlation coefficients in the range 0.57–0.83 (except in Constitución). The simulated directional variability shows good agreement with the directional buoy at Valparaiso station, with a correlation coefficient of 0.68. In general, the MWD shows waves approaching to the coast from the southwest, although some events with waves coming from the west are observed during austral winter. These synoptic changes in the MWD are represented adequately by the model.

The better performance of the SWH compared with MWP can also be appreciated in the scatter plots of the mean values of these variables for all buoys (Figure 4). The simulated mean SWH shows a good agreement with *in situ* observations, but the model has a slight tendency to overestimate the mean SWH with an approximately constant bias of 0.3 m, as shown by the linear regression analysis (Figure 4(a)) consistent with the bias detected previously from satellite measurements. The positive bias observed in MWP (Figure 4(b)) could be attributed essentially to two combined effects; model limitations, as the inadequate
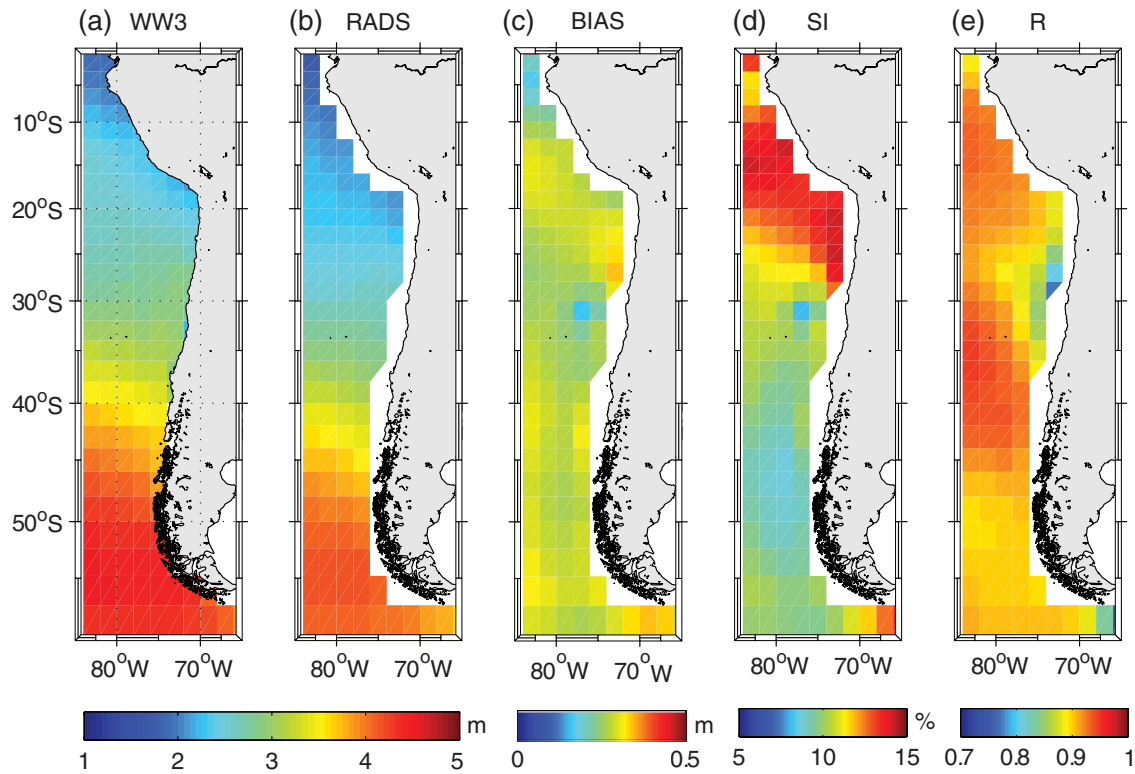
Figure 2. (a) Mean simulated SWH (WW3), (b) mean satellite-derived SWH (RADS), (c) Bias between simulated and satellite SWH (WW3 SWH – RADS SWH), (d) Scatter Index (SI) and (e) correlation coefficient (R). [Colour figure can be viewed at wileyonlinelibrary.com].

Table 3. Statistical comparison between simulated and buoy-measured significant wave height and mean wave period.

Site name	SWH						MWP					
	Bias	RMS	SI	m	b	R	Bias	RMS	SI	m	b	R
32012 (WHOI)	0.42	0.51	19.16	1.00	0.42	0.89	3.08	3.23	31.31	0.99	3.15	0.75
Arica	−0.12	0.30	23.22	0.60	0.44	0.77	1.12	1.57	12.89	0.80	3.35	0.70
Iquique	0.34	0.43	24.75	0.77	0.66	0.80	1.22	1.47	12.08	0.74	4.08	0.71
Antofagasta	0.15	0.31	20.82	0.64	0.63	0.78	2.52	2.84	26.12	0.66	5.34	0.57
Coquimbo	0.68	0.77	35.59	0.76	1.03	0.78	1.05	1.47	13.36	0.75	3.52	0.71
Valparaíso	0.51	0.66	26.88	0.93	0.69	0.85	2.59	2.78	23.96	0.67	5.45	0.83
Constitución	−0.02	0.37	21.49	0.76	0.39	0.83	2.23	2.75	25.29	0.59	5.82	0.44
San Vicente	0.81	0.87	49.15	0.55	1.23	0.43	1.98	2.17	21.42	0.52	5.88	0.58
Chaihuin	0.28	0.75	27.28	0.85	0.67	0.80	0.79	1.28	12.49	0.84	2.30	0.77
Golfo Coronado	0.47	0.73	26.86	0.84	0.82	0.85	1.32	1.68	16.08	0.98	1.50	0.67

swell dissipation used in the physics package (Ardhuin *et al.*, 2010), and topographic features, since they can modify winds and waves at coastal areas.

4. Climatology of the wave field

4.1. Significant wave height

Austral winter June, July and August (JJA) and summer December, January and February (DJF) averages of the simulated SWH (1979–2010) for the Southeast Pacific are presented in Figures 5(a) and (b). The lowest waves are found at the tropical latitudes with mean values of approximately 2 m. The waves progressively increase in

height towards extratropical areas, reaching the highest mean values (>4 m) year-round in the southernmost region (poleward of 45°S). The region of highest waves extends to lower latitudes (∼35°S) during austral winter, as widely reported in global observations and simulations (Young, 1999; Fan *et al.*, 2012). Thus, the seasonal cycle of the SWH (estimated by least-square fitting of an annual harmonic) has maximum amplitude rather far from the coast at approximately 37°S, for both model (Figure 5(c)) and satellite altimetry in RADS and AVISO (Figures 5(d) and (f)). One striking feature is the reduced seasonal variability observed close to the coast of central Chile. In this region, the SWH is approximately 3 m year-round, producing a minimum in the seasonal SWH variability
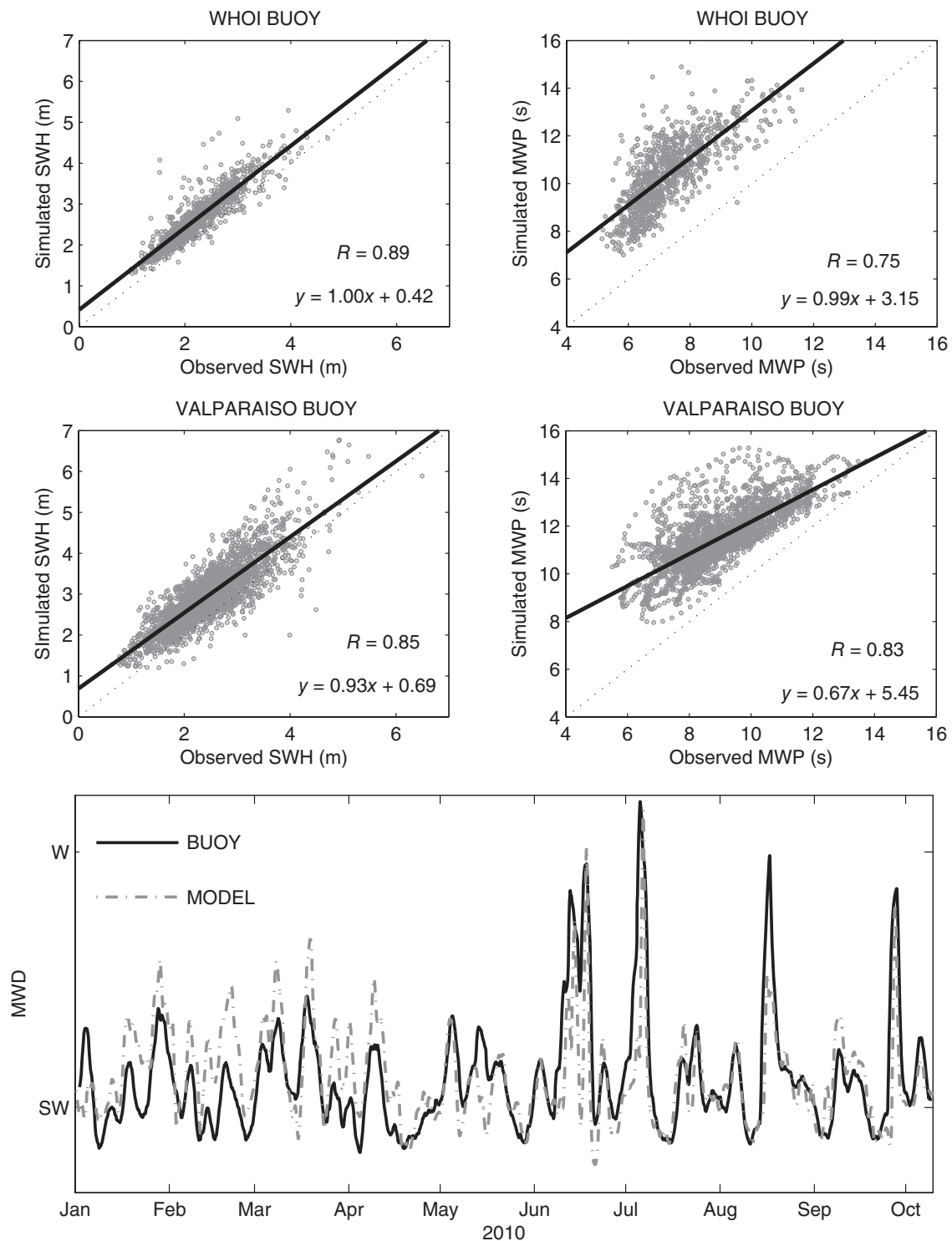
Figure 3. Scatter plots of the simulated and buoy SWH and MWP at the WHOI (upper panel) and Valparaíso (middle panel) stations. Time series of the simulated and buoy MWD at Valparaíso station (lower panel).

(∼0.1 m), which is even lower than that observed south of 45°S. As a climatological feature, this spatial pattern is robust enough to appear in all SWH data sets presented here (as well as in other hindcasts not shown as CAWRC and ERA-Interim) independent of the time period of the climatology. In contrast, off the coast of Peru (∼15°S), where the lowest values of SWH are observed, a secondary maximum in the amplitude of the annual cycle is

suggested in the altimetry data from RADS (Figure 5(d)) and clearly identified in the simulated and AVISO data (Figures 5(c) and (e)).

In order to describe the seasonal variability of SWH over specific regions of the Southeast Pacific, monthly mean values of SWH were calculated for four rectangular regions of 7° of latitude and 4° of longitude that enclose areas off Peru, central Chile offshore, central
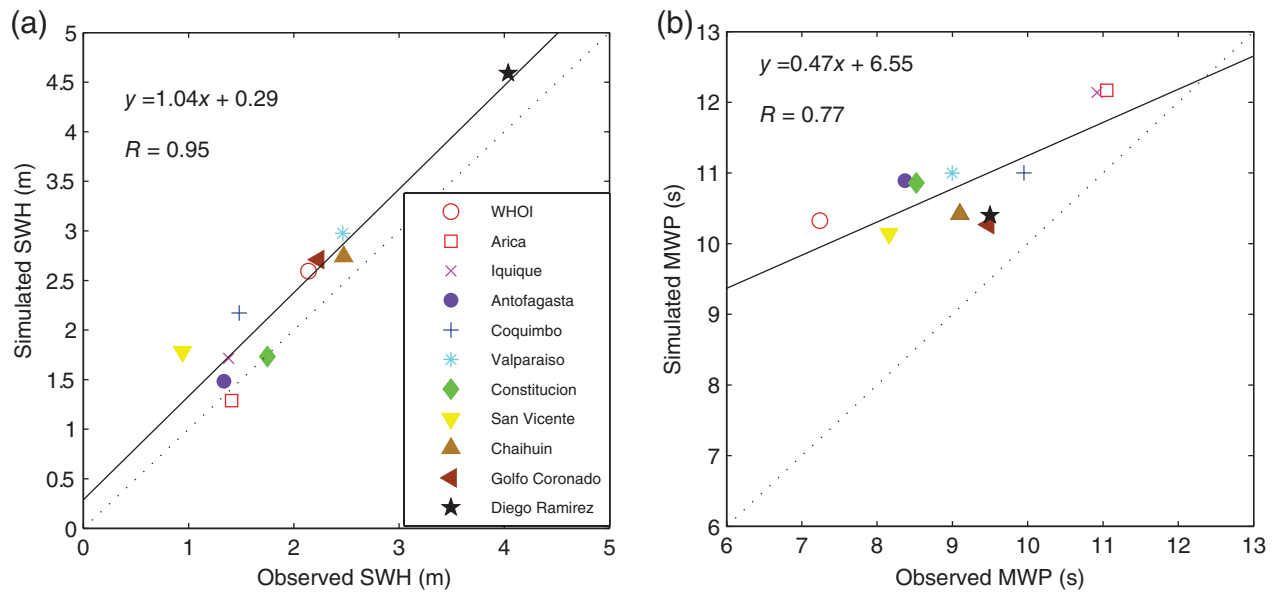
Figure 4. Scatter plots of mean simulated and mean observed wave parameters using all available buoys. (a) SWH and (b) MWP. [Colour figure can be viewed at wileyonlinelibrary.com].

Chile near-shore and Patagonia (Figure 1). The monthly mean SWH within each region and its spatial and temporal (interannual) standard deviation are shown in Figure 6. Off the coast of Peru the annual cycle of the simulated and the satellite SWH data follow the same pattern reaching a maximum during the austral winter and early spring. However, the annual cycle of the simulated data is more pronounced than in satellite data (as seen previously in maps), mainly because of the simulation of higher waves during the peak season (Figure 6(a)). As mentioned above, the annual cycle is much weaker near the coastal region of central Chile, the region of lowest seasonal variability in the Southeast Pacific coast, where the seasonal variation of the SWH is rather flat with mean values around 3 m (Figure 6(b)). Offshore of central Chile the SWH shows strong seasonal variability with maximum SWH during late fall and austral winter and good agreement between simulated and satellite SWH data (Figure 6(c)). In contrast, off the Patagonia region the monthly mean values of the SHW do not show a clear annual cycle, but a slight semi-annual cycle with maxima during April and August (Figure 6(d)). Although the simulated data show higher waves than satellite data, the structure of the climatology is very similar in all four regions.

4.2. Wind sea and swell SWH

The austral winter (JJA) and summer (DJF) mean of SWH (1979–2010) related to wind sea (SWH_{sea}) and swell (SWH_{swell}), obtained using the spectral partitioning method, are shown in Figure 7. In general, maps of the SWH_{sea} illustrate a large-scale seasonal pattern similar to that of the SWH, with lower waves equatorward of 33°S (~1 m) and the highest waves at higher latitudes, with values exceeding 3 m. Nevertheless, at a regional scale, secondary maxima of the SWH_{sea} (~2 m) are clearly evident off the coast of Peru (~15°S) during austral winter,

and off the coast of central Chile (~33°S) during austral summer. These zones coincide with the well-known locations of the coastal jets off Peru and Central Chile, as can also be appreciated from the 7 m s^{-1} wind speed contours shown on the maps (Figure 7(a)). These regional maxima in the SWH_{sea} have a significant impact on the seasonal cycle, reaching maximum amplitude far from the coast off central Chile (~37°S), and just off the coast of Peru, consistent with the maximum amplitudes of the annual cycle of the observed and simulated SWH. However, near the coast of central Chile (~33°S), SWH_{sea} shows another regional maximum of the amplitude of its annual cycle with values of approximately 1 m, which contrasts with the reduced seasonal variability of the total SWH discussed in the previous section.

The austral winter and summer mean of the SWH (1979–2010) of remotely forced waves (SWH_{swell}) show a more uniform spatial pattern with wave heights between 1.5 and 3 m over almost the entire study domain (Figure 7(b)). The highest values are found around 37°S and SWH_{swell} decreases both northward and southward of this latitude. The seasonal pattern involves an extension of the area of higher waves during austral winter, which progressively decreases until austral summer when wave heights are reduced in most of the region. In general, the amplitude of the annual cycle of the SWH_{swell} is smaller when compared with the SWH_{sea}. However, there is a notable increase in the amplitude of the seasonal cycle over the coastal region of central Chile as a result of a sharp decrease in SWH_{swell} during summer. The physical meaning of this feature is difficult to assess and is likely to be related to the limitations of the spectral partitioning method, as discussed in Section 5.

The monthly mean values of SWH_{sea} and SWH_{swell} are shown for the four regions of the Southeast Pacific in Figure 6. The monthly means of the SWH_{sea} are lower
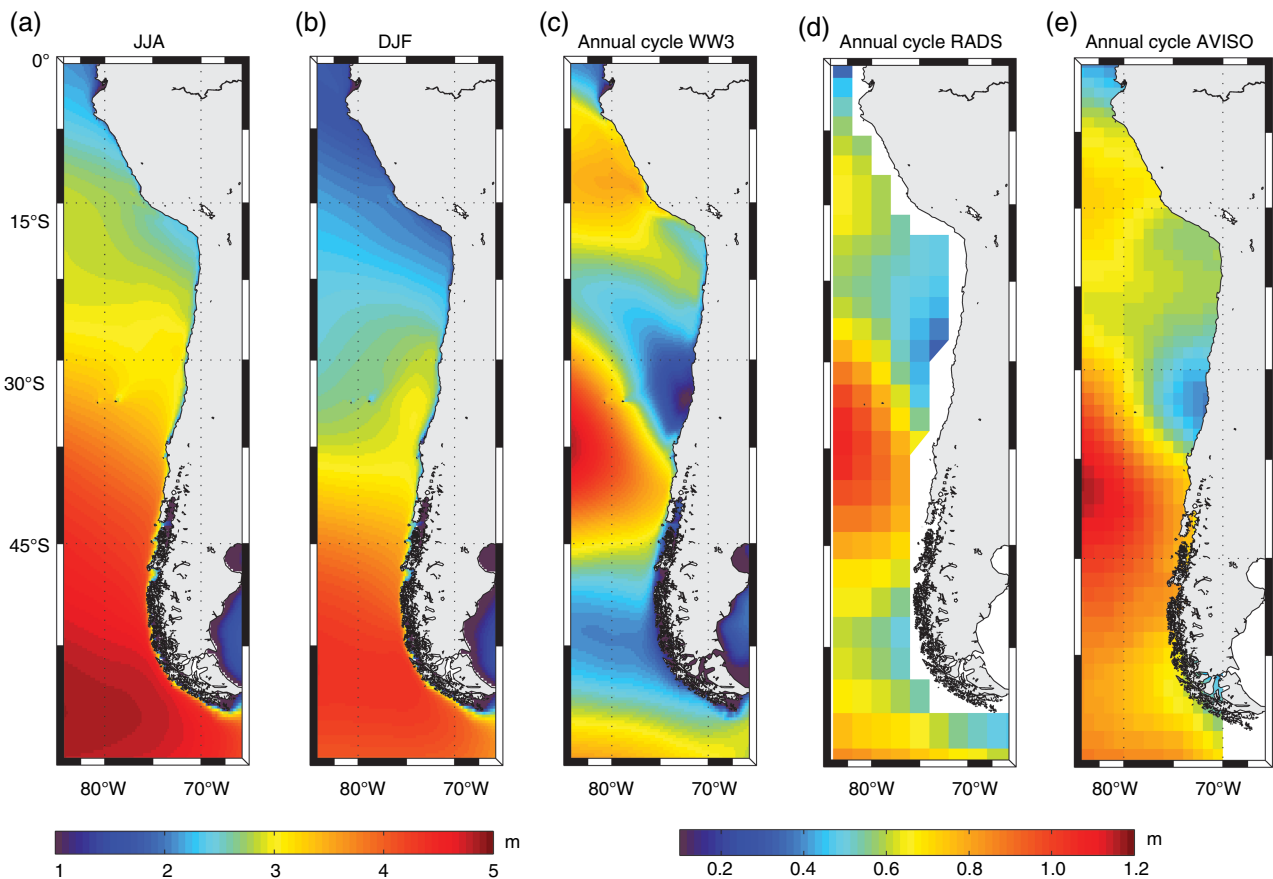
Figure 5. Seasonal mean (1979–2010) of simulated SWH for (a) austral winter (JJA) and (b) summer (DJF). Amplitude of the annual cycle of SWH from (c) simulation (1979–2010), (d) RADS data (1992–2014) and (e) AVISO data (2009–2015). [Colour figure can be viewed at wileyonlinelibrary .com].

than the SWH_{swell} off Peru (Figure 6(a)) and central Chile (Figures 6(b) and (c)). However, seasonal variability of the SWH_{sea} is more pronounced than SWH_{swell} at the coastal region of Peru (Figure 6(a)) and the offshore region in central Chile (Figure 6(c)). Thus, in spite of having lower mean values, SWH_{sea} seasonality is essential for the development of an annual cycle in the SWH at both these areas, due to higher values during austral winter. In contrast, over the coastal region of central Chile, the amplitude of the annual cycles of SWH_{sea} and SHW_{swell} are very similar, but with opposite phase (Figure 6(b)), SWH_{sea} being higher during the austral summer and SHW_{swell} during the winter. These opposite seasonal patterns explain the markedly flat annual cycle of the satellite and simulated SWH. Thus, in this region the SWH_{sea} also plays an important role in modulating the annual cycle of the SWH, in this case decreasing its amplitude. Off the Patagonia region, the SWH_{sea} is slightly higher than SHW_{swell} and both seem to play a role in the reduced seasonal variation observed in the SWH.

4.3. Mean wave period and mean wave direction of propagation

The austral winter and summer averages (1979–2010) of the MWP and MWD of propagation of the Southeast Pacific are presented in Figure 8. It is important to note that MWP is very uniform in space and time with values

between 9 and 12 s over the whole study domain. However, it is possible to observe seasonal changes in the MWP associated with the presence of wind sea conditions, which are characterized by shorter periods. Thus, spatial patterns and seasonal variability of the MWP show an inverse behaviour to that of SWH_{sea}. In general, shorter mean periods are found at higher latitudes and longer periods at lower latitudes, but this spatial pattern is disrupted by the presence of wind sea conditions at the coastal-jet regions of Peru and central Chile, where the mean period decreases during austral winter-spring and spring-summer, respectively.

The MWD is essentially constant through the year. The general spatial pattern consists of westerly waves southward of 45°S and southwesterly waves northward of 45°S. Only a slight seasonal variation is observed off the coast of Peru, with a more southerly direction of propagation in winter (vectors in Figure 8).

The most remarkable feature of the MWD_{sea} distribution is the predominance of local southerly waves along the Southeast Pacific coast north of approximately 30°S, which expands to higher latitudes (~37°S) during summer (not shown). In addition, southeasterly MWD_{sea} are more frequent offshore, consistent with the trade wind regime, and close to the coast of Peru (~15°S) during winter (along-shore winds). At higher latitudes waves come
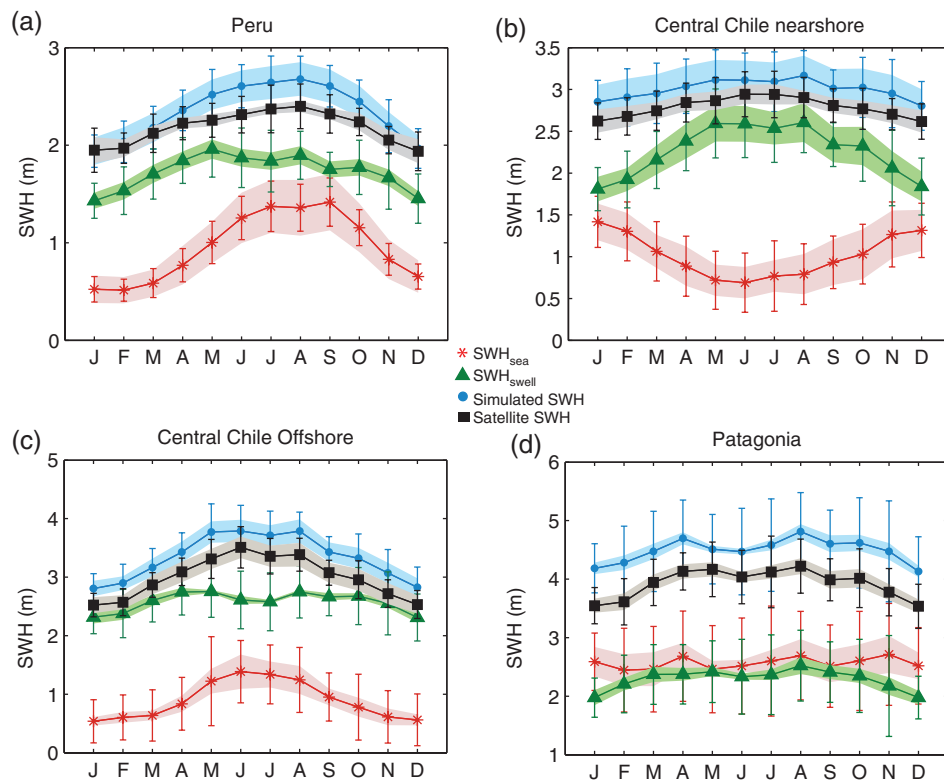
Figure 6. Climatology of the satellite SWH (squares), simulated SWH (dots), simulated SWH_{sea} (asterisk) and simulated SWH_{swell} (triangles) at four regions of the Southeast Pacific. (a) Peru, (b) central Chile near-shore, (c) central Chile offshore and (d) Patagonia. The shaded areas are the spatial standard deviation of SWH and bars are the temporal standard deviation of SWH. [Colour figure can be viewed at wileyonlinelibrary.com].

essentially from the west, southwest and northwest, following the westerlies wind belt and associated disturbances. This regime extends towards lower latitudes during the austral winter. Northerly waves also appear in this season along the coast of southern Chile (35°–50°S) which are absent during summer.

On the other hand, most swell waves come from the southwest north of 45°S, with no significant differences between winter and summer. The second most frequent direction is from the south, especially off Peru during summer. Farther south, as was the case for MWD_{sea}, swell waves come essentially from the west, southwest and northwest (not shown).

5. Discussion and conclusions

In this work, we have presented a detailed wind wave climatology for the Southeast Pacific based on a 32-year simulation using the WaveWatch III model. We have placed particular emphasis on the characterization of the amplitude of the annual cycle of SWH and the annual variation of sea state, using a spectral partitioning method. The annual mean SWH exhibits clearly the pattern of the surface wind circulation, the most prominent feature being the presence of the westerlies at 40°–60°S, where the stronger winds lead to the local generation of waves which propagate as swells throughout the ocean basin. As such, a meridional variation of mean wave intensity, with higher SWH in the south and lower SWH to the north, dominates

over the study area. Wintertime strengthening and northward migration of the westerlies lead to generally higher SWH in this season. However, in this study we have found that satellite and simulated SWH, as well as the simulated MWP, show regional variability that is closely associated with the spatial patterns and seasonality of synoptic-scale atmospheric low-level coastal jets off the coasts of Peru and Central Chile. The existence of these enhanced wind regions shows a strong relationship with the amplitude of the annual cycle of the SWH along the coast. In the case of Peru, the coastal jet is strongest in austral winter, leading to an amplification of the seasonal variability of SWH, whereas off Central Chile the coastal winds are strongest during spring-summer so that locally generated waves are out phase with swell, leading to a suppressed annual cycle with nearly constant SWH throughout the year. Thus, our results support the idea that regional atmospheric features, such as coastal low-level jets, modify the sea state in terms of a seasonal modulation of the SHW energy ratio from wind sea and swell. This regional feature has been noted in all four eastern boundary current systems (Semedo *et al.*, 2011), where strong atmospheric low-level jets are a common feature (Strub *et al.*, 2013). This modulation of the SHW annual cycle in the Southeast Pacific by coastal wind jet seasonality appears also as a robust feature in satellite data.

Although the major conclusions of this research are unlikely to be affected by the spectral partitioning method to isolate wind sea and swell wave types, it is of interest
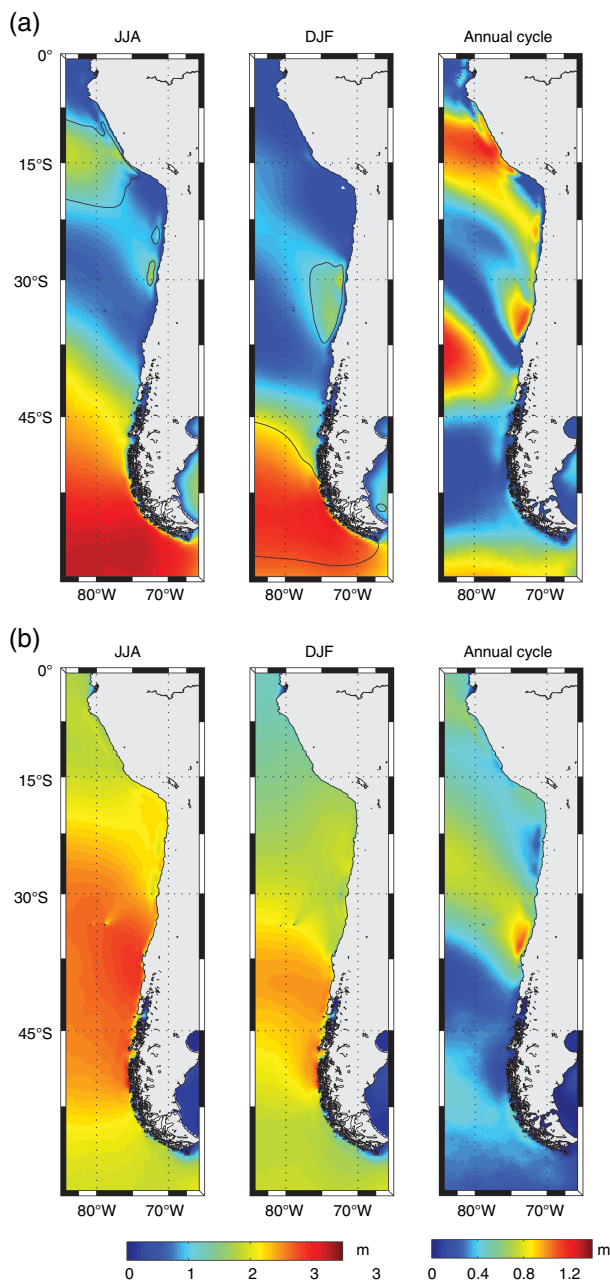
(a)

(b)

Figure 7. (a) Seasonal mean (1979–2010) of SWH_{sea} for austral winter (JJA), summer (DJF) and the amplitude of the annual cycle. The continuous lines indicate a mean wind speed of 7 ms^{-1}. (b) Seasonal mean (1979–2010) of SWH_{swell} for austral winter (JJA), summer and the amplitude of the annual cycle of SWH_{swell}. [Colour figure can be viewed at wileyonlinelibrary.com].

to discuss its limitations. The wave age criterion used here (Hanson and Phillips, 2001), is based on the directional spectra and wind information, and has been widely used in the past for the climatological characterization of wave types. For example, this method was used by the CAWCR wave hindcast (Durrant *et al.*, 2013) and by Fan *et al.*, 2014 to assess global changes in wind sea and swell under climate change scenarios. Nevertheless, it is important to note that this method of partitioning of the spectrum may have difficulties distinguishing wind sea and swell when these waves come from similar directions. In this case, the
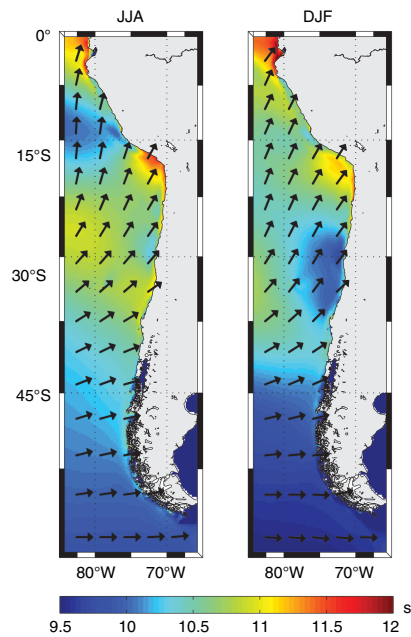

Figure 8. Seasonal mean (1979–2010) of the simulated MWP and MWD for austral winter (JJA) and summer (DJF). [Colour figure can be viewed at wileyonlinelibrary.com].

method becomes one-dimensional and its accuracy will depend on whether the wind sea and swell have clearly separated peak frequencies. As the wave frequencies generated in high wind speeds approach those of the underlying swell wave (∼0.1–0.05 Hz), the method is expected to have difficulties in high-wind situations when the wind direction is similar to the predominant swell direction.

In order to examine in more detail, the ability of the spectral partitioning method to distinguish between wind sea and swell in our study area, Figure 9 shows two-dimensional wind speed and direction histograms for winter (JJA) and summer (DJF), along with the energy differences between summer and winter in the directional wave spectrum for three locations: near-shore Peru (10°S–80°W), near-shore Central Chile (33°S–73°W) and offshore Central Chile (30°–80°S). Off Peru the winds are highly concentrated in the S–SE direction with moderate speeds in winter (∼7 m s^{-1}, Figure 9(a)) and weaker ones in summer (∼5 m s^{-1}, Figure 9(b)). The associated seasonal variation in the wave spectrum (Figure 9(c)) is seen as a broad region of higher wintertime wave energy in the S–SE direction at frequencies between 0.1 and 0.2 Hz. This is clearly differentiated from the swell-related seasonality, which produces a second region of higher wintertime energy at lower frequency (∼0.06 Hz) within the SW–S directional range. In contrast, near-shore central Chile (Figures 9(d)–(f)) an important summertime increase of energy at higher frequencies (0.1–0.2 Hz) is observed (Figure 9(f)) associated with a local increase in southerly winds during summer (Figure 9(e)). Given that southerly wind events during summer can reach speeds of ∼15 m s^{-1} with significant synoptic-scale and diurnal variability (Rahn and Garreaud, 2013), we expect these winds to have an impact in the wave directional spectrum
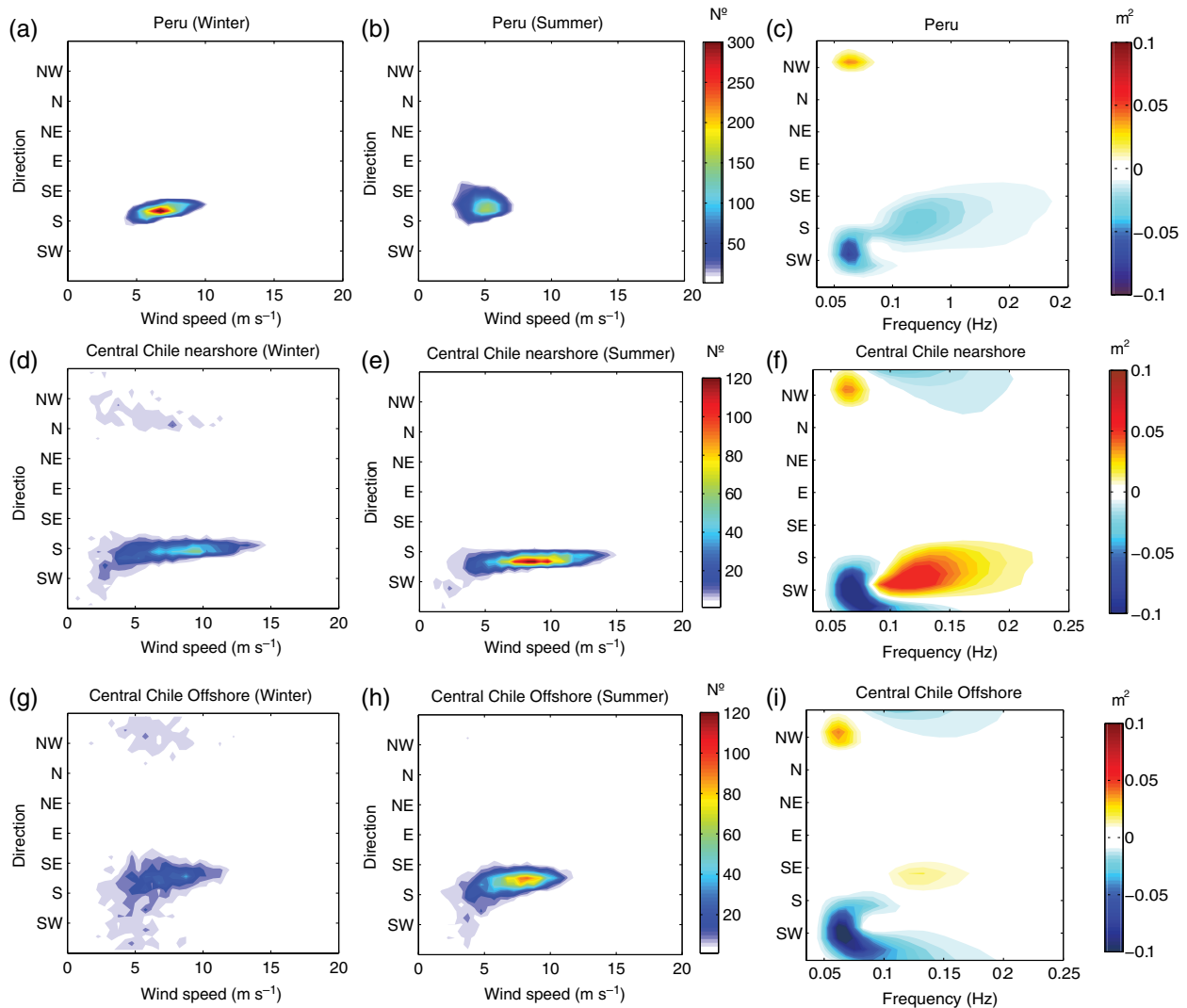
Figure 9. Two-dimensional histogram (number of events) of the wind speed and direction for winter (a, d, g) and summer (b, e, h). The rightmost figures (c, f, i) show the difference between summer mean and winter mean wave energy (m^2) in the directional spectra. The data locations are shown in Figure 1. [Colour figure can be viewed at wileyonlinelibrary.com].

over a broad range of frequencies (Figure 9(f)). In this sense, this seasonal wind intensification off central Chile could generate southerly wind sea waves that cannot be adequately differentiated from swell waves coming from the southwest in the spectral data. As a result, it is probable that the sharp decrease in swell-related SWH (SWH_{swell}) during summer, and the consequent increase in the annual cycle off the coast of central Chile observed in Figure 8 may be partly or wholly due to a miss-assignation of swell and wind sea states when the coastal winds become strong enough to generate wave frequencies that might be confused with swell. At the offshore location (Figures 9(g)–(i)) the winds are generally weaker, oriented SE and show a reduced seasonal variation. As such, the summertime wave energy maximum is weaker and more clearly separated from the swell related winter maximum at this location (Figure 9(i)).

Another possible source of seasonal variability is the summertime presence of swell propagating from the NW direction, generated by storms in the northern hemisphere.

This swell source appears as a NW summer energy maximum at 0.07 Hz at all three of the locations shown in Figure 9. However, the energy input associated with this wave source is smaller and of similar magnitude for Peru and Chile (near-shore and offshore) suggesting that this swell component does not contribute significantly to the regional variability observed in SWH.

Several global studies of future changes in wind-wave climate have been performed due their broad implications for the operation and design of coastal infrastructure, for marine renewable energy and for coastal environmental issues (Fan *et al.*, 2013, Hemer *et al.*, 2013a; Hemer *et al.*, 2013b; Semedo *et al.*, 2013). Fan *et al.* (2014) predict large-scale changes in wind sea and swell as response to anthropogenic change. For example, they found that wind sea energy will increase in the Southern Ocean as the southern annular mode shifts towards its positive phase (Guillett and Fyfe, 2013). This will lead to an increase of the SWH at the Southern Ocean and a corresponding decrease in the South Pacific mid-latitudes,

particularly during the austral summer (Hemer *et al.*, 2013a). Energy ratios between wind sea and swell could also change as coastal jets shift meridionally in accordance with the projections of atmospheric surface circulation (Semedo *et al.*, 2016; Soares *et al.*, 2016). Thus, regional projections of coastal low-level jets will be necessary to adequately evaluate changes in the sea state off Chile and Perú and in other coastal areas where wind jets are present.

Acknowledgements

References

Aguirre C, Pizarro O, Strub T, Garreaud R, Barth J. 2012. Seasonal dynamics of the alongshore flow off central Chile. *J. Geophys. Res.* **117**: C01006. https://doi.org/10.1029/2011JC007379.

Aguirre C, Garreaud R, Rutllant J. 2014. Surface ocean response to synoptic-scale variability in wind stress and heat fluxes off south-central Chile. *Dyn. Atmos. Oceans* **65**: 64–85. https://doi.org/10.1016/j.dynatmoce.2013.11.00.

Allan J, Komar PD. 2000. Are ocean wave heights increasing in the eastern North Pacific? *EOS Trans. Am. Geophys. Union* **81**: 561–567.

Alves JH. 2006. Numerical Modeling of swell contributions to the global wind-wave climate. *Ocean Model.* **11**: 98–122. https://doi.org/10.1016j.ocemod.2004.11.007.

Ardhuin F, Rogers E, Babanin A, Filipot J-F, Magne R, Roland A, van der Westhuysen A, Queffeulou P, Lefevre J-M, Aouf L, Collard F. 2010. Semi-empirical dissipation source functions for wind-wave models: part I, definition, calibration and validation. *J. Phys. Oceanogr.* **40**(9): 1917–1941.

Babanin AV. 2011. *Breaking and Dissipation of Ocean Surface Waves*. Cambridge University Press, 480.

Battjes JA, Janssen J. 1978. Energy loss and set-up due to breaking of random waves. In *Proceedings of 16th International Conference on Coastal Engineering*, ASCE, 569–558.

Bosserelle C, Pattiaratchi C, Haigh I. 2011. Inter-annual variability and longer-term changes in the wave climate of Western Australia between 1970 and 2009. *Ocean Dyn.* **61**: 63–76.

Cavaleri L, Fox-Kemper B, Hemer M. 2012. Wind-waves in the coupled climate system. *Bull. Am. Meteorol. Soc.* **93**: 1651–1661. https://doi.org/10.1175/BAMS-D-11-00170.1.

Challenor PG, Cotton PD. 2002. The joint calibration of altimeter and in-situ wave heights. Technical Report No. 13, World Meteorological Organization document number WMO/TD-No.1081, JCOMM.

Chawla A, Tolman HL. 2007. Automated grid generation for WAVE-WATCH III. Technical note 254, NCEP/NOAA/NWS.

Chawla A, Spindler D, Tolman HL. 2013. Validation of a thirty year wave hindcast using the climate forecast system reanalysis winds. *Ocean Model.* **70**: 189–206.

Chelton DB, Hussey KJ, Parke ME. 1981. Global satellite measurements of water vapor, wind speed and wave height. *Nature* **294**: 529–532.

Cox AT, Swail VR. 2001. A global wave hindcast over the period 1958–1997: validation and climate assessment. *J. Geophys. Res.* **106**: 2313–2329.

Dewitte B, Illig S, Renault L, Goubanova K, Takahashi K, Gushchina D, Mosquera K, Purca S. 2011. Modes of covariability between sea surface temperature and wind stress intraseasonal anomalies along the coast of Peru from satellite observations (2000 – 2008). *J. Geophys. Res.* **116**: C04028. https://doi.org/10.1029/2010JC006495.

Dodet G, Bertin X, Taborda R. 2010. Wave climate variability in the North-East Atlantic Ocean over the last six decades. *Ocean Model.* **31**: 120–131.

Donelan MA, Drennan WM, Kasaros KB. 1997. The air–sea momentum flux in conditions of wind sea and swell. *J. Phys. Oceanogr.* **27**: 2087–2099. https://doi.org/10.1175/1520-0485(1997)027,2087: TASMFI.2.0.CO;2.

Durrant T, Hemer M, Trenham C, Greenslade D. 2013. *CAWCR Wave Hindcast 1979–2010*. v7. CSIRO. Data Collection. https://doi.org/10.4225/08/523168703DCC5.

Fan Y, Ginis I, Hara T. 2009. The effect of wind–wave–current interaction on air–sea momentum fluxes and ocean response in hurricanes. *J. Phys. Oceanogr.* **39**: 1019–1034. https://doi.org/10.1175/2008JPO4066.1.

Fan Y, Lin SJ, Held IM, Yu Z, Tolman HL. 2012. Global ocean surface wave simulation using a coupled atmosphere–wave model. *J. Clim.* **25**: 6233–6252. https://doi.org/10.1175/JCLI-D-11-00621.1.

Fan Y, Held IM, Lin SJ, Wang X. 2013. Ocean warming effect on surface gravity wave climate change for the end of the twenty-first century. *J. Clim.* **26**: 6046–6066. https://doi.org/10.1175/JCLI-D-12-00410.1.

Fan Y, Lin SJ, Griffies SM, Hemer M. 2014. Simulated global swell and wind-sea climate and their responses to anthropogenic climate change at the end of the twenty-first century. *J. Clim.* **27**: 3516–3536. https://doi.org/10.1175/JCLI-D-13-00198.1.

Garreaud R, Munoz R. 2005. The low-level jet off the subtropical west coast of South America: structure and variability. *Mon. Weather Rev.* **133**: 2246–2261.

Garreaud R, Rutllant J, Fuenzalida H. 2002. Coastal lows in north-central Chile: mean structure and evolution. *Mon. Weather Rev.* **130**: 75–88.

Gorman RM, Bryan KR, Laing AK. 2003. Wave hindcast for the New Zealand region: deep-water wave climate. *N. Z. J. Mar. Freshw. Res.* **37**: 589–612.

Guilliet NP, Fyfe JC. 2013. Annular mode changes in the CMIP5 simulations. *Geophys. Res. Lett.* **40**: 1189–1193. https://doi.org/10.1002/grl.50249.

Gulev SK, Grigorieva V, Sterl A, Woolf D. 2003. Assessment of the reliability of wave observations from voluntary observing ships: insights from the validation of a global wind wave climatology based on voluntary observing ship data. *J. Geophys. Res. Oceans* **108**(C7): 3236. https://doi.org/10.1029/2002JC001437.

Hanson JL, Phillips OM. 2001. Automated analysis of ocean surface directional wave spectra. *J. Atmos. Oceanic. Technol.* **18**: 277–293. https://doi.org/10.1175/1520-0426(2001)018,0277:AAOOSD.2.0.CO;2.

Hasselmann K, Barnett TP, Bouws E, Carlson H, Cartwright DE, Enke K, Ewing JA, Gienapp H, Hasselmann DE, Kruseman P, Meerburg A, Mueller P, Olbers DJ, Richter K, Sell W, Walden H. 1973. Measurements of wind-wave growth and swell decay during the Joint North Sea Wave Project (JONSWAP). Ergaenzungsheft zur Deutschen Hydrographischen Zeitschrift, Reihe A(8) 12, 95 pp.

Hasselmann S, Hasselmann K, Allender JH, Barnett TP. 1985. Computations and parametrizations of the nonlinear energy transfer in a gravity-wave spectrum, Part II: parametrizations of the nonlinear energy transfer for applications in wave models. *J. Phys. Oceanogr.* **15**: 1378–1391.

Hasselmann S, Hasselmann K, Bruning C. 1994. Extraction of wave spectra from SAR image spectra. In *Dynamics and Modelling of Ocean Waves*, Komen G *et al.* (eds). Cambridge University Press, 391–401.

Hemer MA, Church JA, Hunter JR. 2010. Variability and trends in the directional wave climate of the Southern Hemisphere. *Int. J. Climatol.* **30**: 475–491. https://doi.org/10.1002/joc.1900.

Hemer MA, Fan Y, Mori N, Semedo A, Wang XL. 2013a. Projected future changes in wave climate from a multi-model ensemble. *Nat. Clim. Chang.* **3**: 471–476. https://doi.org/10.1038/NCLIMATE1791.

Hemer MA, Katzfey J, Trenham CE. 2013b. Global dynamical projections of surface ocean wave climate for a future high greenhouse gas emission scenario. *Ocean Model.* **70**: 221–245. https://doi.org/10.1016/j.ocemod.2012.09.008.

Izaguirre C, Mendez F, Menendez M, Losada IJ. 2011. Global extreme wave height variability based on satellite data. *Geophys. Res. Lett.* **38**: L10607. https://doi.org/10.1029/2011GL047302.

Komar P. 1997. *Beach processes and sedimentation*. Prentice-Hall: New Jersey, USA.

Laing AK. 2000. New Zealand wave climate from Satellite observations. *N. Z. J. Mar. Freshw. Res.* **34**: 727–744.

Mediavilla D, Sepuvelda H. 2016. Nearshore assessment of wave energy resources in central Chile (2009–2010). *Renew. Energy* **90**: 136–144. https://doi.org/10.1016/j.renene.2015.12.066.

Pizarro O, Hormazábal S, González A, Yañez E. 1994. Variabilidad del viento, nivel del mar y temperatura en la costa norte de Chile. *Investig. Mar.* **22**: 85–101.

Queffeulou P. 2004. Long-term validation of wave height measurements from altimeters. *Mar. Geod.* **27**: 495–510.

Rahn D, Garreaud R. 2013. A synoptic climatology of the near-surface wind along the west coast of South America. *Int. J. Climatol.* **34**: 780–792. https://doi.org/10.1002/joc.3724.

Rascle N, Ardhuin F. 2013. A global wave parameter database for geophysical applications. Part 2: model validation with improved source term parameterization. *Ocean Model.* **70**: 174–188.

Reistad M, Breivik Ø, Haakenstad H, Aarnes OJ, Furevik BR, Bidlot JR. 2011. A high-resolution hindcast of wind and waves for the North Sea, the Norwegian Sea, and the Barents Sea. *J. Geophys. Res.* **116**: C05019. https://doi.org/10.1029/2010JC006402.

Renault L, Dewitte B, Falvey M, Garreaud R, Echevin V, Bonjean F. 2009. Impacts of atmospheric coastal jet off central Chile on SST from satellite observations (2000-2007). *J. Geophys. Res.* **114**: C08006. https://doi.org/10.1029/2008JC005083.

Renault L, Dewitte B, Marchesiello P, Illig S, Echevin V, Cambon G, Ramos M, Astudillo O, Minnis P, Ayers K. 2012. Upwelling response to atmospheric coastal jets off central Chile: a modeling study of the October 2000 event. *J. Geophys. Res.* **117**: C02030. https://doi.org/10.1029/2011JC007446.

Saha S, Moorthi S, Pan H, Wu X, Wang J, Nadiga S, Tripp P, Kistler R, Wollen J, Behringer D, Liu H, Stokes D, Grumbine R, Gayno G, Wang J, Hou Y, Chuang H, Juang H, Sela J, Iredell M, Treadon R, Kleist D, Delst PV, Keyser D, Derber J, Ek M, Meng J, Wei H, Yang R, Lord S, Van den Dool H, Kumar A, Wang W, Long C, Chelliah M, Xue Y, Huang B, Schemm J, Ebisuzaki W, Lin R, Xie P, Chen M, Zhou S, Higgins W, Zou C, Liu Q, Chen Y, Han Y, Cucurull L, Reynolds R, Rutledge G, Goldberg M. 2010. The NCEP climate forecast system reanalysis. *Bull. Am. Meteorol. Soc.* **91**: 1015–1057.

Scharroo R, Leuliette EW, Lillibridge JL, Byrne D, Naeije MC, Mitchum GT. 2013. RADS: Consistent multi-mission products. In Proceedings of the Symposium on 20 Years of Progress in Radar Altimetry, Venice, 20-28 September 2012, Eur. Space Agency Spec. Publ., ESA SP-710.

Semedo A, Suselj K, Rutgersson A, Sterl A. 2011. A global view on the wind sea and swell climate and variability from ERA-40. *J. Clim.* **24**: 1461–1479. https://doi.org/10.1175/2010JCLI3718.1.

Semedo A, Weisse R, Beherens A, Sterl A, Bengtson L, Günther H. 2013. Projection of global wave climate change toward the end of the twenty-first century. *J. Clim.* **26**: 8269–8288. https://doi.org/10.1175/JCLI-D-12-00658.1.

Semedo A, Soares PMM, Lima DCA, Cardoso RM, Bernardino M. 2016. The impact of climate change on the global low-level wind jets: EC-EARTH simulations. *Glob. Planet Change* **137**: 88–106. https://doi.org/10.1016/j.gloplacha.2015.12.012.

Skamarock WC, Klemp JB, Dudhia J, Gill DO, Barker DM, Duda MG, Huang X-Y, Wang W, Powers JG. 2008. A Description of the Advanced Research WRF Version 3. NCAR Technical Note NCAR/TN-475+STR, 113 pp. https://doi.org/10.5065/D68S4MVH.

Soares PMM, Lima DCA, Cardoso R, Semedo A. 2016. High resolution projections for the western Iberian coastal low level jet in a changing climate. *Clim. Dyn.* https://doi.org/10.1007/s00382-016-3397-8.

Sterl A, Caires S. 2005. Climatology, variability and extrema of ocean waves: The web-based KNMI/ERA-40 wave atlas. *Int. J. Climatol.* **25**: 963–977.

Sterl A, Komen GJ, Cotton PD. 1998. Fifteen years of global wave hindcasts using winds from the European Centre for Medium-Range Weather Forecast reanalysis: Validating the reanalyzed winds and assessing the wave climate. *J. Geophys. Res.* **103**: 5477–5492.

Stopa JE, Ardhuin F, Babanin A, Zieger S. 2016. Comparison and validation of physical wave parameterizations in spectral wave models. *Ocean Model.* **103**: 2–17. https://doi.org/10.1016/j.ocemod.2015.09.003.

Strub PT, Combes V, Shillington FA, Pizarro O. 2013. Currents and Processes along the Eastern Boundaries. In *Ocean Circulation and Climate - A 21st Century Perspective*. Academic Press, 339–384.

Tolman HL. 2008. A mosaic approach to wind wave modeling. *Ocean Model.* **25**: 35–47.

Tolman HL. 2009. User manual and system documentation of WAVE-WATCH III version 3.14. Technical Note 276, NOAA/NWS/NCEP/MMAB, 220 pp. EONOTP.2.0.CO;2.

Tolman HL, Chalikov D. 1996. Source terms in a third generation wind wave model. *J. Phys. Oceanogr.* **26**: 2497–2518.

Tracy B, Devaliere EM, Nicolini T, Tolman HL, Hanson JL. 2007. Wind sea and swell delineation for numerical wave modeling. *Proceedings of the 10th International Workshop on Wave Hindcasting and Forecasting and Coastal Hazard Symposium*. U.S. Army Engineer Research & Development Center.

Woolf DK, Challenor PG, Cotton PD. 2002. Variability and predictability of the North Atlantic wave climate. *J. Geophys. Res.* **107**: 3145–3158. https://doi.org/10.1029/2001JC001124.

Young IR. 1999. Seasonal variability of the global ocean wind and wave climate. *Int. J. Climatol.* **19**: 931–950. https://doi.org/10.1002/(SICI)1097-0088(199907)19:9<931::AID-JOC412>3.0.CO;2-O.

Young IR, Zieger S, Babanin AV. 2011. Global trends in wind speed and wave height. *Science* **332**: 451–455. https://doi.org/10.1126/science.1197219.